The Astronomical Journal, 130:2529–2540, 2005 December

VLBI OBSERVATIONS OF SOUTHERN HEMISPHERE ICRF SOURCES. II. ASTROMETRIC SUITABILITY BASED ON INTRINSIC STRUCTURE

Roopesh Ojha,[1] Alan L. Fey,[2] Patrick Charlot,[3] David L. Jauncey,[1] Kenneth J. Johnston,[2] John E. Reynolds,[1] Anastasios K. Tzioumis,[1] Jonathan F. H. Quick,[4] George D. Nicolson,[4] Simon P. Ellingsen,[5] Peter M. McCulloch,[5] and Yasuhiro Koyama[6]

Received 2005 April 12; accepted 2005 August 21

ABSTRACT

We present 8.4 GHz very long baseline interferometry (VLBI) observations of 48 southern hemisphere extragalactic sources from the International Celestial Reference Frame. These are the second in a series of observations intended to image all such sources in the southern hemisphere at milliarcsecond resolution and bring the total number of observed sources to 111. We use these data, together with previously published data, to quantify the magnitude of the expected effect of intrinsic source structure on astrometric bandwidth synthesis VLBI observations by calculating a "structure index" for the sources; the structure index yields an estimate of their astrometric quality. Approximately 35% of sources in our sample have a structure index indicative of compact or very compact structures. The remaining two-thirds of our sources are less compact and should probably be avoided in astrometric and geodetic VLBI experiments requiring the highest accuracy unless intrinsic source structure can be accounted for in the astrometric/geodetic analysis.

Key words: astrometry — galaxies: active — quasars: general — radio continuum: galaxies — reference systems — surveys

Online material: machine-readable tables

1. INTRODUCTION

Dual frequency very long baseline interferometry (VLBI) observations at 8.4 GHz (X band) and 2.3 GHz (S band) have been used since the late 1970s to determine the positions of compact radio sources with milliarcsecond accuracy. The use of two frequencies allows the calibration of the frequency-dependent propagation delay in the ionosphere, with the basic observable being the group delay. This technique has been employed to make observations of selected strong, compact, extragalactic radio sources to define, maintain, and improve a radio reference frame with submilliarcsecond precision. Johnston et al. (1988) set out to establish a global celestial reference frame of 400 sources in 1986. The first catalog (Ma et al. 1990) had 182 sources with a positional accuracy of 1 mas, with all sources located north of -30° declination. Subsequent observing campaigns increased the density of sources in the northern hemisphere and added sources in the southern hemisphere (Russell et al. 1994; Reynolds et al. 1994; Johnston et al. 1995).

The current realization of the celestial frame is the International Celestial Reference Frame (ICRF; Ma et al. 1998), which was adopted by the XXIII IAU General Assembly in 1997 to replace the traditional FK5 optical fundamental reference system as the fundamental celestial reference frame. The ICRF source positions are estimated to be accurate to the 0.25 mas level. The ICRF replaced the stellar FK5 as the fundamental celestial reference frame as of 1998 January 1 and is the realization of the International Celestial Reference System (ICRS) at radio wavelengths with a precision of approximately 20 μas in each coordinate axis. The *Hipparcos* catalog (Perryman et al. 1997) is the realization of the ICRS at optical wavelengths (Kovalevsky et al. 1997). There have been two extensions (Fey et al. 2004c) of the ICRF, which provide positions for an additional 109 extragalactic sources added since the ICRF was defined.

Extragalactic radio sources are known to have extended emission structure that varies both spatially and temporally on scales of months to years. This departure from the static point-source approximation, commonly made in astrometric analysis, introduces errors in the observable quantities of group delay and delay rate. Charlot (1990) showed that the effect of source structure on VLBI astrometric positions can be significant. Also, as the structure of these sources varies with time it is important to image their structure at several epochs in order to determine internal proper motions and hence define a time-dependent source model. Multiepoch Very Long Baseline Array (VLBA) observations to image northern hemisphere sources at 8.4 GHz have been progressing successfully; 90% of the ICRF sources north of -20° declination have been imaged (Fey & Charlot 2000). However, many of the southern hemisphere sources in the ICRF (Ma et al. 1998) had not been imaged in detail at the milliarcsecond level, particularly those south of -30° declination. We have undertaken a comprehensive imaging study of all 184 southern hemisphere ICRF sources that had not been previously imaged at milliarcsecond scales.

We have used the Australian Long Baseline Array (LBA), augmented by telescopes in South Africa, Hawaii, and Japan, to image 48 ICRF sources at a radio frequency of 8.4 GHz. These are the second set of results from a multiepoch observing program that seeks to image, at least twice, all existing southern hemisphere ICRF sources, as well as new additions being made

[1] Australia Telescope National Facility, CSIRO, P.O. Box 76, Epping, NSW 1710, Australia.
[2] United States Naval Observatory, 3450 Massachusetts Avenue NW, Washington, DC 20392-5420.
[3] Observatoire de Bordeaux (OASU)—CNRS/UMR 5804, BP 89, 33270 Floirac, France.
[4] Hartebeesthoek Radio Astronomy Observatory, P.O. Box 443, Krugersdorp 1740, South Africa.
[5] School of Mathematics and Physics, University of Tasmania, Private Bag 37, Hobart, Tasmania 7001, Australia.
[6] Kashima Space Research Center, Communications Research Laboratory, 893-1 Hirai, Kashima, Ibaraki 314-8501, Japan.

TABLE 1
THE LONG BASELINE ARRAY

Telescope	Diameter (m)	8.4 GHz System Equivalent Flux Density (Jy)	Location
Parkes	64	90	Parkes, New South Wales
ATCA	5×22	80	Narrabri, New South Wales
Mopra	22	400	Coonabarabran, New South Wales
Hobart	26	750	Mt. Pleasant, Tasmania
Ceduna	30	600	Ceduna, South Australia
Hartebeesthoek[a]	26	560	Hartebeesthoek, South Africa
Kokee[a]	20	900	Kokee Park, Hawaii, USA
Kashima[a]	34	300	Ibaraki, Japan

[a] Affiliated telescopes.

as part of our astrometry program (Fey et al. 2004a, 2004b). Images of 69 sources were reported in Ojha et al. (2004b, hereafter Paper I).

As the first comprehensive milliarcsecond imaging survey of extragalactic sources in the southern hemisphere, our program greatly extends existing limited surveys (Preston et al. 1989; Shen et al. 1997, 1998). In addition to yielding source structure information for astrometric purposes, in most cases these are the first VLBI images of these flat-spectrum, extragalactic sources. Past experience, e.g., the Pearson-Readhead Survey and follow-up surveys (Taylor et al. 1996; Pearson & Readhead 1988), shows that such extensive surveys are a powerful tool not only for astrometry but also for the investigation of a wide range of astrophysical phenomena. Astrophysical dividends from this ongoing survey have begun (Ojha et al. 2004a).

Based on the initial work of Charlot (1990) and following the analysis of Fey & Charlot (2000), we have used our LBA images of 111 sources to estimate the contribution of the extended emission structure of the observed sources, measured at a single epoch, to the astrometric quantities used to determine VLBI positions. The results reported here provide an indicator of the astrometric quality of each source and constitute a continuing effort toward the long-term maintenance and improvement of the ICRF.

2. OBSERVATIONS

The observations reported in this paper were made using the five telescopes that make up the Australian LBA,[7] as well as telescopes in South Africa, Hawaii, and Japan. Details of these telescopes are summarized in Table 1. Due to limited mutual visibility between telescopes in South Africa, Hawaii, and Japan, a typical observing epoch is split into two sessions, one involving observation with the LBA and South Africa and the other involving observation with the LBA, Hawaii, and occasionally Kashima. The data from each session are calibrated separately and then combined to give the best possible (u, v)-plane coverage. Images from three epochs are presented here. The first epoch consisted of a 40 hr session with the LBA and the Hartebeesthoek Radio Astronomy Observatory on 2003 June 20. The second epoch consisted of a 24 hr session with the LBA and Hartebeesthoek on 2003 November 23, followed by a 24 hr session with the LBA, Kokee, and Kashima on 2003 November 24. The third epoch consisted of a 24 hr session with the LBA and Hartebeesthoek on 2004 April 18 and 20 and a 24 hr session with the LBA, Kokee, and Kashima on 2004 April 19.

At our observing frequency of 8.4 GHz, the LBA in these configurations yielded a *typical* angular resolution (synthesized beam) 1.5 mas $\times$ 0.7 mas in size, with the highest resolution in the east-west direction. Each source was observed with about eight scans of approximately 12 minutes each. After accounting for slew time, the *typical* total on-source time was about 75 minutes.

The data were recorded in S2 format (Cannon et al. 1997) and correlated at the Australia Telescope National Facility (ATNF) correlator located in Epping, NSW (Wilson et al. 1995). These data have only one intermediate frequency (IF)[8] with a bandwidth of 8 MHz per polarization. The correlated data were processed using the NRAO's Astronomical Image Processing System (AIPS) software (Bridle & Greisen 1994; Greisen 1988). The data were loaded into AIPS using the locally written task *atlod*, which is needed to read the data in the format that the LBA generates. Thereafter, data inspection, initial editing, and fringe fitting were done in the standard manner using AIPS.

Overall amplitude calibration was improved using observations of known sources with $\geq$90% of their correlated flux in a compact core. A single amplitude gain correction factor was derived for each antenna based on fitting a simple Gaussian source model to the visibility data of the respective compact source after applying only the initial calibration based on the measured system temperatures and gain curves. Gain correction factors were calculated based on the differences between the observed and model visibilities. The resulting set of amplitude gain correction factors was then applied to the visibility data of the target sources. Finally, the visibility data were Fourier inverted and CLEANed using the Caltech DIFMAP package (Shepherd 1997). The data were self-calibrated following the hybrid imaging technique of Pearson & Readhead (1984) to correct for residual amplitude and phase errors.

3. RESULTS

Contour plots of the final, naturally weighted images of the 48 sources are shown in Figure 1. Six of these 48 sources, PKS 0522−611, PKS 0738−674, PKS 0925−203, PKS 1057−797, PKS 1519−273, and PKS 1908−201, have also been observed previously in Paper I. The average rms noise in the images is $\sim$1.1 mJy beam^{-1}, with a median rms of $\sim$0.8 mJy beam^{-1}. Table 2 lists parameters of all the images. Following the source name, the next three columns list the major axis, minor axis, and

[7] The Long Baseline Array is part of the Australia Telescope, which is funded by the Commonwealth of Australia for operation as a National Facility managed by CSIRO.

[8] In this context "intermediate frequency" refers to a single signal path between a telescope and the correlator. In general, the total bandpass is divided into IFs that are adjacent in freqency. IFs should be distinguished from the narrow spectral channels into which they are subdivided, as the geometrical and propagation errors affecting the data can be large enough to cause significant phase changes across an IF bandwidth.

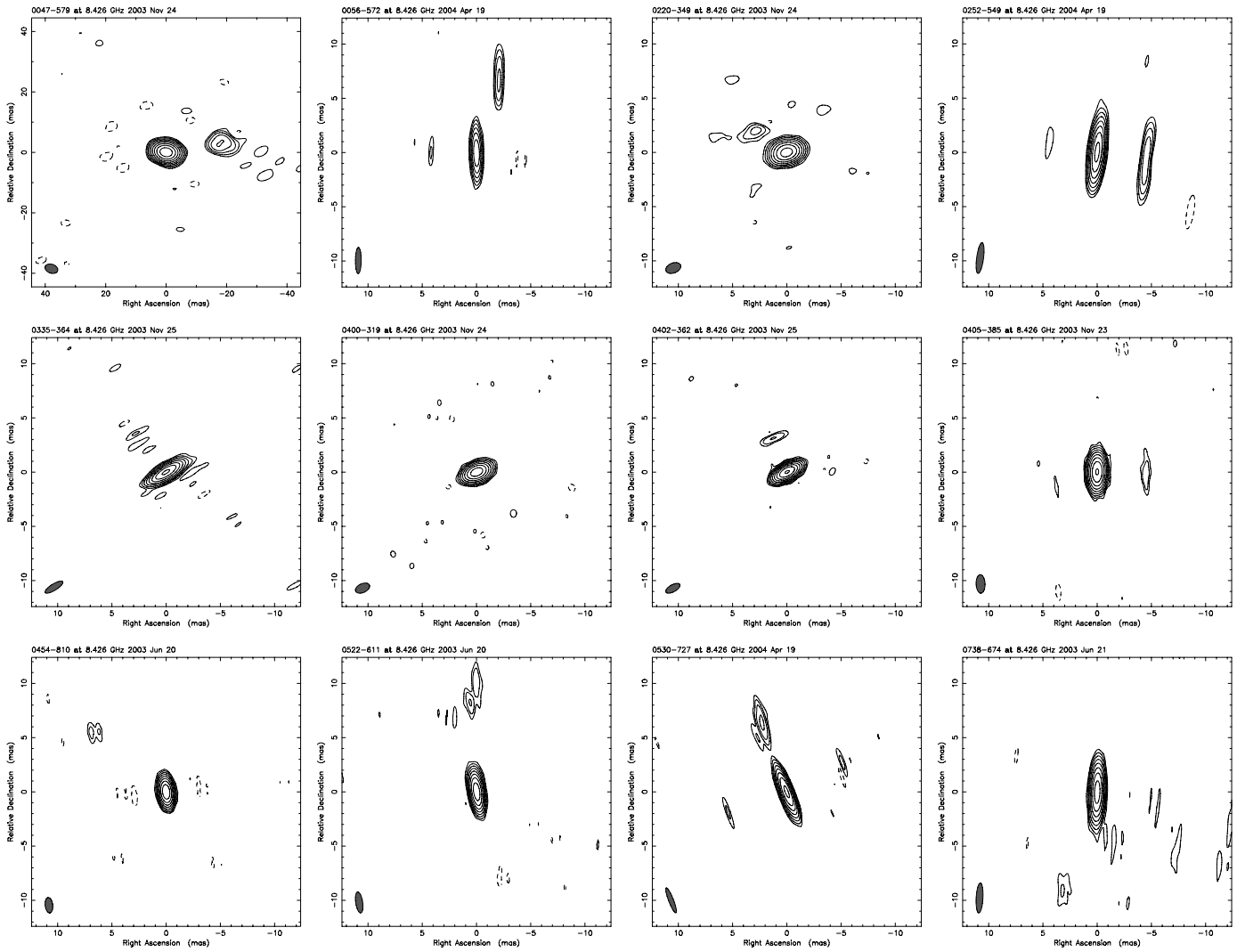

FIG. 1.—Contour plots of 48 extragalactic radio sources at 8.4 GHz. Image parameters are listed in Table 2. Gaussian models fitted to the visibility data are listed in Table 3. The scale of each image is in milliarcseconds. The FWHM Gaussian restoring beam applied to the images is shown as a crosshatched ellipse in the lower left of each panel.

position angle of the beam. The next two columns list the peak and rms flux densities of the image. The final column indicates the contour levels used for each image.

The Australian LBA is an ad hoc array, and as such, the locations of the individual elements of this array are not optimal for the generation of uniform (*u, v*)-coverage. This restricted sampling in the (*u, v*)-plane (see Fig. 3, Paper I) is the most important limitation on image quality. One important check on the robustness of our images is to compare the images of sources that are mutually visible to the VLBA and the LBA. This was done for 12 sources in Paper I, and in every case our images were found to be consistent with those from the VLBA.[9] Another useful check, also performed in Paper I, was to compare sources imaged at multiple epochs. All nine sources for which we have images at two or more epochs show consistent structures between those epochs. These results suggest that our images are morphologically robust, reliable, and repeatable.

The distribution of source (VLBI) flux density is shown in Figure 2. Values range from a minimum of 50 mJy to a maximum of 2.3 Jy. The mean flux density is 0.62 Jy with a median of 0.44 Jy. With our 8 MHz bandwidth and 3 minute fringe fit interval, the rms 1 σ sensitivity for our most sensitive baseline, Parkes to the phased Australia Telescope Compact Array (ATCA, five of six dishes), is 0.32 mJy.

Gaussian models were fitted to the self-calibrated *visibility data* using the Caltech DIFMAP package. The results of the model fitting are listed in Table 3. After the source name the following items are listed: component number, total component flux, distance of component from core, orientation of component with respect to the core component, length of major axis of component, axial ratio[10] of component (1 for circular component), and orientation of major axis of component. By inspection of the images and these fitted models we can loosely classify the morphology of the sources into two groups. Fifteen sources exhibit a compact structure with a single fitted component. The remaining 33 sources exhibit complex, multiple-component structure.

[9] The VLBA images can be found in the USNO Radio Reference Frame Image Database at http://rorf.usno.navy.mil/rrfid.shtml.

[10] Circular model components were the default choice, with elliptical model components being used when circular model components clearly did not provide a good fit.

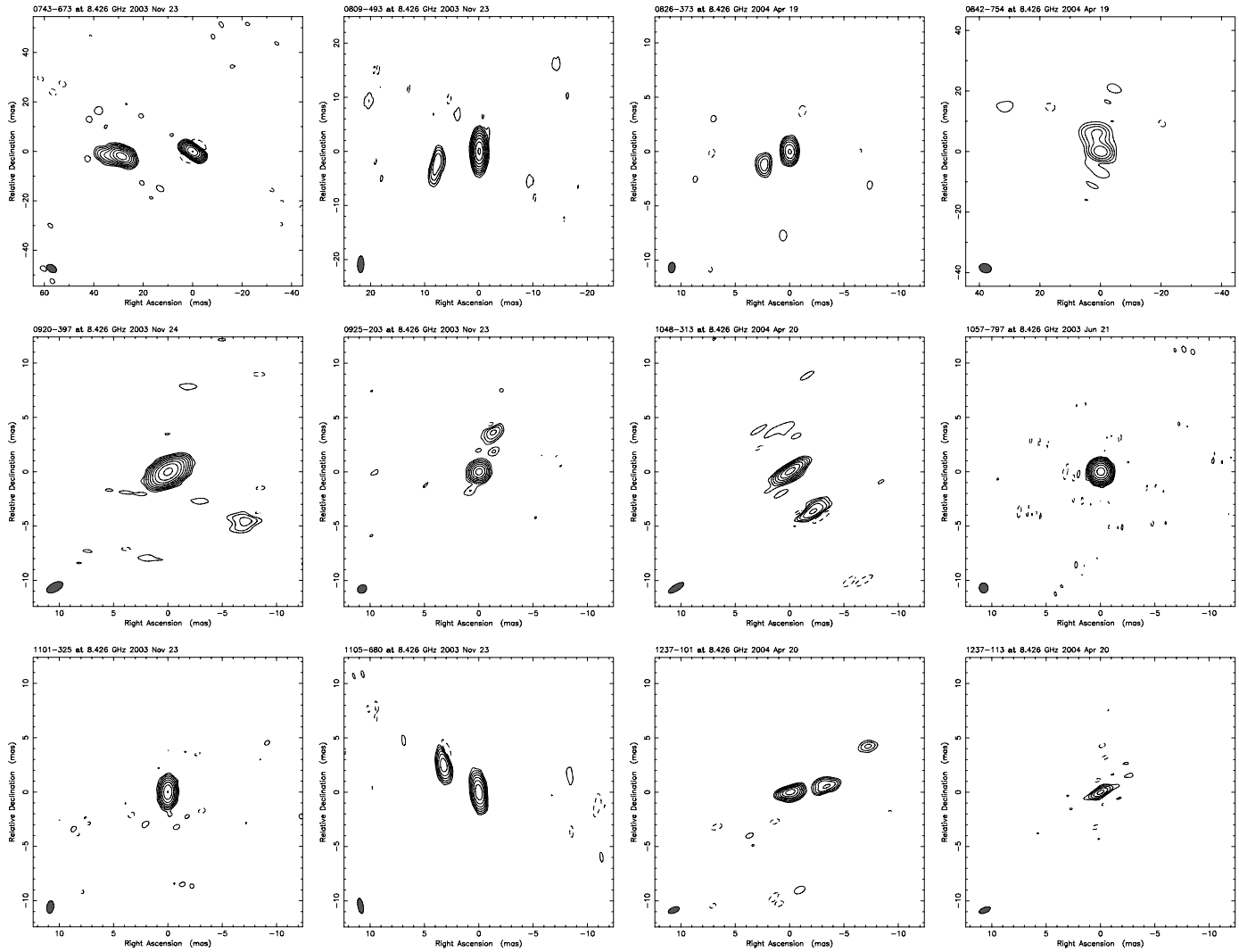

FIG. 1.—*Continued*

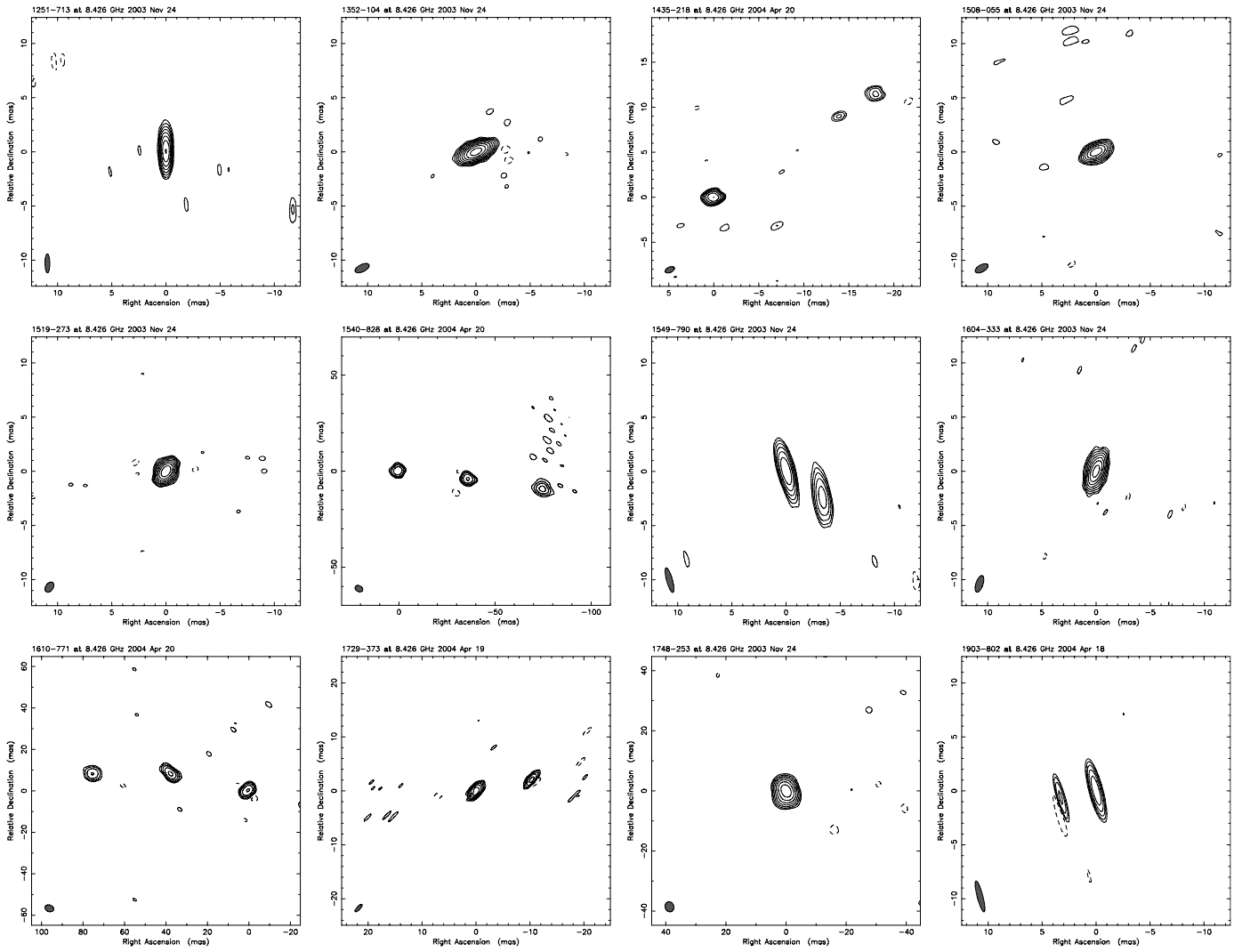

FIG. 1.—*Continued*

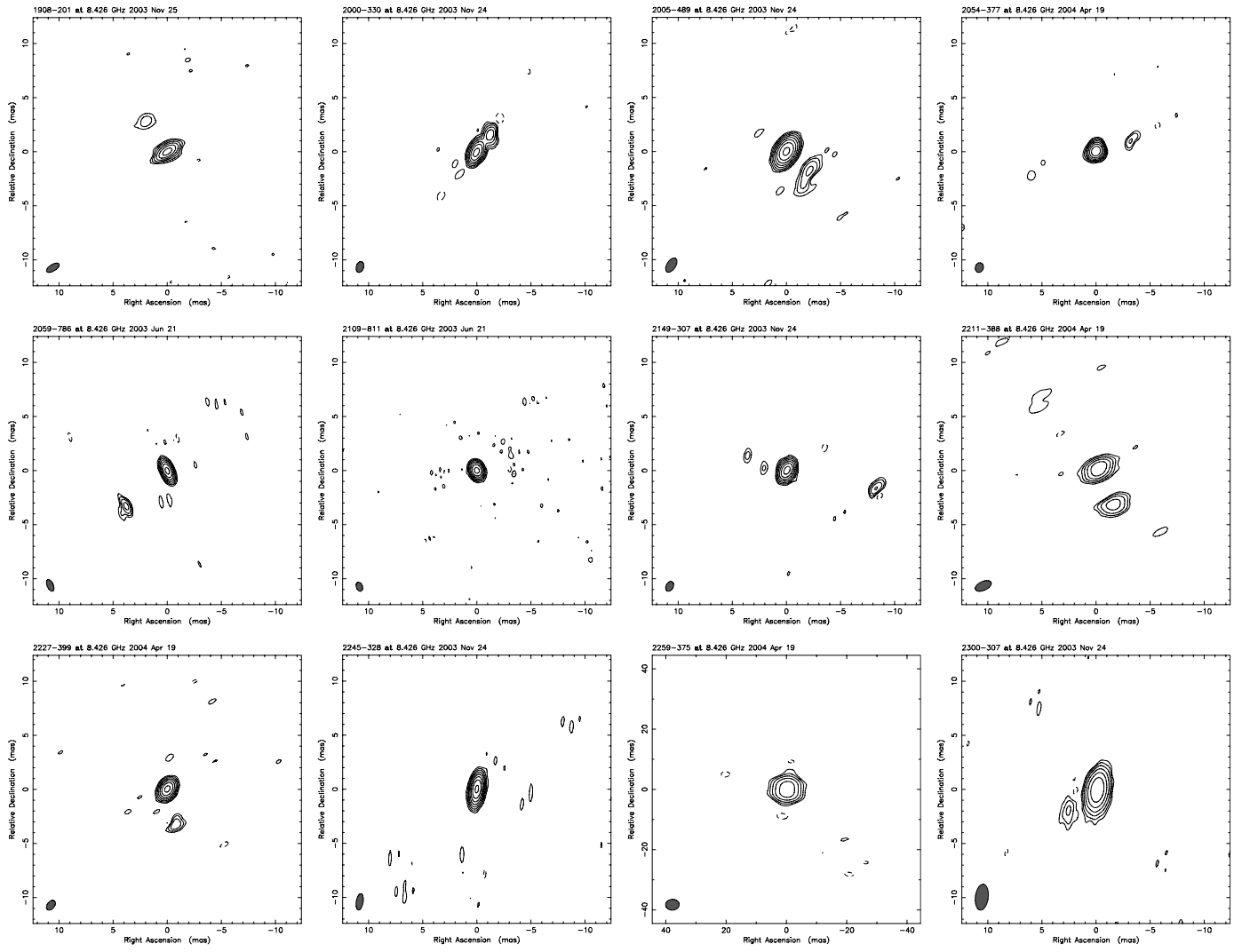

FIG. 1.—*Continued*

TABLE 2
PARAMETERS OF NATURALLY WEIGHTED IMAGES

SOURCE	BEAM[a]			PEAK[b]	rms[c]	CONTOUR LEVELS[d]
	a (mas)	b (mas)	ϕ (deg)	(Jy beam^{-1})	(mJy beam^{-1})	(mJy beam^{-1})
0047−579	4.3	3.0	71	0.86	0.7	$2.0\times(1,\ldots,2^8)$
0056−572	2.4	0.5	0	0.14	0.4	$2.4\times(1,\ldots,2^5)$
0220−349	1.4	0.9	−68	0.59	0.9	$3.2\times(1,\ldots,2^7)$
0252−549	2.9	0.6	−8	0.66	1.0	$4.0\times(1,\ldots,2^7)$
0335−364	1.9	0.6	−58	0.24	0.5	$1.7\times(1,\ldots,2^7)$
0400−319	1.4	0.8	−66	0.52	0.8	$2.5\times(1,\ldots,2^7)$
0402−362	1.5	0.6	−61	2.10	1.9	$7.7\times(1,\ldots,2^8)$
0405−385	1.7	0.8	2	1.01	1.0	$3.6\times(1,\ldots,2^8)$
0454−810	1.4	0.7	7	0.76	1.1	$3.2\times(1,\ldots,2^7)$
0522−611	2.0	0.6	8	0.38	0.6	$1.8\times(1,\ldots,2^7)$
0530−727	2.5	0.4	21	0.21	0.3	$1.4\times(1,\ldots,2^7)$
0738−674	2.8	0.6	−3	0.18	0.3	$1.0\times(1,\ldots,2^7)$
0743−673	4.4	2.8	58	0.56	0.4	$1.1\times(1,\ldots,2^9)$
0809−493	3.1	1.2	−2	0.30	0.3	$1.1\times(1,\ldots,2^8)$
0826−373	1.0	0.6	−7	0.53	1.9	$7.6\times(1,\ldots,2^6)$
0842−754	4.1	3.0	76	0.07	0.7	$2.3\times(1,\ldots,2^4)$
0920−397	1.6	0.8	−62	0.84	0.9	$2.8\times(1,\ldots,2^8)$
0925−203	0.9	0.7	−58	0.17	0.6	$2.0\times(1,\ldots,2^6)$
1048−313	1.6	0.6	−58	0.22	0.6	$2.6\times(1,\ldots,2^6)$
1057−797	0.9	0.8	10	1.05	0.8	$2.8\times(1,\ldots,2^8)$
1101−325	1.2	0.6	−9	0.26	0.7	$2.0\times(1,\ldots,2^7)$
1105−680	1.4	0.5	10	0.36	1.1	$3.4\times(1,\ldots,2^6)$
1237−101	1.1	0.5	−68	0.45	1.2	$4.7\times(1,\ldots,2^6)$
1237−113	1.1	0.5	−68	0.07	0.9	$3.2\times(1,\ldots,2^4)$
1251−713	1.7	0.4	1	0.28	0.7	$2.1\times(1,\ldots,2^7)$
1352−104	1.4	0.7	−64	0.90	0.8	$2.3\times(1,\ldots,2^8)$
1435−218	1.1	0.6	−67	0.27	0.9	$4.2\times(1,\ldots,2^6)$
1508−055	1.3	0.7	−61	0.52	1.6	$4.8\times(1,\ldots,2^6)$
1519−273	1.0	0.7	−35	1.18	1.6	$4.7\times(1,\ldots,2^7)$
1540−828	4.2	3.1	60	0.05	0.9	$3.1\times(1,\ldots,2^4)$
1549−790	2.3	0.5	15	0.48	2.9	$7.9\times(1,\ldots,2^5)$
1604−333	1.6	0.6	−18	0.17	0.3	$0.9\times(1,\ldots,2^7)$
1610−771	4.3	3.2	69	0.33	3.6	$17.8\times(1,\ldots,2^4)$
1729−373	1.8	0.6	−43	0.22	1.1	$4.3\times(1,\ldots,2^5)$
1748−253	3.4	2.9	18	0.11	0.3	$1.0\times(1,\ldots,2^6)$
1903−802	2.9	0.5	15	0.17	1.8	$5.5\times(1,\ldots,2^4)$
1908−201	1.3	0.6	−58	0.96	7.3	$21.8\times(1,\ldots,2^5)$
2000−330	1.0	0.7	−17	0.25	0.6	$3.0\times(1,\ldots,2^6)$
2005−489	1.5	0.8	−32	0.43	0.9	$2.8\times(1,\ldots,2^7)$
2054−377	0.9	0.7	−15	0.37	0.6	$3.0\times(1,\ldots,2^6)$
2059−786	1.2	0.6	24	0.17	0.7	$2.1\times(1,\ldots,2^6)$
2109−811	0.9	0.6	20	0.26	1.0	$3.1\times(1,\ldots,2^6)$
2149−307	1.0	0.7	−29	0.56	1.6	$6.4\times(1,\ldots,2^6)$
2211−388	1.6	0.8	−66	0.12	1.0	$3.9\times(1,\ldots,2^4)$
2227−399	1.0	0.7	−39	0.25	0.8	$3.1\times(1,\ldots,2^6)$
2245−328	1.5	0.6	−9	0.19	0.4	$1.3\times(1,\ldots,2^7)$
2259−375	4.5	3.6	−89	0.08	0.7	$2.9\times(1,\ldots,2^4)$
2300−307	2.4	1.2	−7	0.08	0.4	$1.3\times(1,\ldots,2^5)$

[a] The restoring beam is an elliptical Gaussian with FWHM major axis a and minor axis b, with major axis in position angle ϕ (measured north through east).

[b] Amplitude gain correction factors were typically at the 10% level but were often as high as 20%.

[c] The rms of the residuals of the final hybrid image.

[d] Contour levels are represented by the geometric series $1, \ldots, 2^n$, e.g., for $n = 5$ the contour levels would be ± 1, 2, 4, 8, 16, and 32.

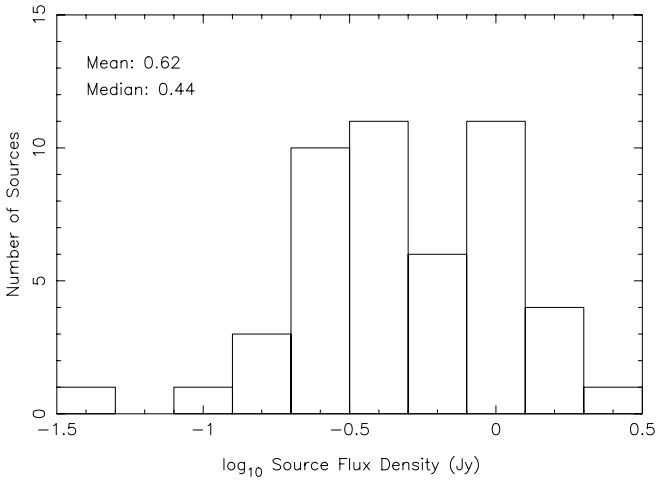

FIG. 2.—Distribution of source flux density for the 48 observed ICRF sources. Total flux density is defined as the total CLEANed flux density (i.e., the sum of all CLEAN components).

The physical characteristics of all sources, where available, are summarized in Table 4, which lists their optical identification and redshift, as well as visual magnitude. This information was obtained from the NASA/IPAC Extragalactic Database (NED).

4. DISCUSSION

In this section we attempt to quantify the expected effects of intrinsic source structure on astrometric bandwidth synthesis VLBI observations. As shown by Charlot (1990), the contribution of intrinsic source structure to a VLBI bandwidth synthesis delay measurement can be significant and depends on the exact form of the spatial brightness distribution of the extended radio source relative to the geometry of the VLBI baseline vector projected onto the plane of the sky. The overall source structure effect for a given source is most easily estimated by calculating corrections to the bandwidth synthesis delay, based on the observed source structure, for a range of (u, v)-coordinates (the coordinates u and v are the coordinates of the baseline vector projected onto the plane of the sky and are expressed in units of the observing wavelength). Following such a scheme, Fey & Charlot (1997) defined a source "structure index" according to the median value of the structure delay corrections, $\tau_{\rm median}$, calculated for all projected VLBI baselines that could be possibly observed with Earth-based VLBI [i.e., for all baselines with $(u^2 + v^2)^{1/2}$ less than the diameter of the Earth], separating the sources into four classes as follows:

$$\text{Structure Index} = \begin{cases} 1, & 0 \text{ ps} \le \tau_{\rm median} < 3 \text{ ps}, \\ 2, & 3 \text{ ps} \le \tau_{\rm median} < 10 \text{ ps}, \\ 3, & 10 \text{ ps} \le \tau_{\rm median} < 30 \text{ ps}, \\ 4, & 30 \text{ ps} \le \tau_{\rm median} < \infty. \end{cases}$$

The structure index can be used as an estimate of the astrometric quality of the sources. The interested reader is referred to Fey & Charlot (1997) for a more detailed description of the structure index definition and to Charlot (1990) for a more thorough discussion of the algorithm used to calculate source structure effects in the VLBI group delay observable.

In addition to the original analysis of Fey & Charlot (1997), Fey & Charlot (2000) calculated X-band structure indices for an additional 225 sources. Based on their analysis of 389 mostly

TABLE 3
GAUSSIAN MODELS[a]

Source	Component No.	S (Jy)	r (mas)	θ (deg)	a (mas)	b/a	ϕ (deg)
0047−579	1	1.064	0.0	...	2.17	0.51	−67
	2	0.077	18.7	−80	3.94	1.00	...
0056−572	1	0.156	0.0	...	0.29	1.00	...
	2	0.043	7.0	−19	1.90	1.00	...
0220−349	1	0.729	0.0	...	0.52	1.00	...
	2	0.040	1.9	69	0.34	1.00	...
0252−549	1	0.750	0.0	...	0.29	1.00	...
	2	0.071	4.7	−103	0.66	1.00	...
0335−364	1	0.288	0.0	...	0.33	1.00	...
	2	0.017	1.9	−72	0.36	1.00	...
0400−319	1	0.565	0.0	...	0.28	1.00	...
0402−362	1	2.280	0.0	...	0.25	1.00	...
	2	0.026	3.4	23	0.02	1.00	...
0405−385	1	1.099	0.0	...	0.36	1.00	...
	2	0.012	4.4	−80	0.00	1.00	...
0454−810	1	0.777	0.0	...	0.13	1.00	...
0522−611.....	1	0.403	0.0	...	0.19	1.00	...
	2	0.013	7.8	−2	0.29	1.00	...
0530−727	1	0.273	0.0	...	0.38	1.00	...
	2	0.027	6.6	22	1.91	1.00	...
0738−674	1	0.204	0.0	...	0.28	1.00	...
0743−673	1	0.538	0.0	...	0.00	1.00	...
	2	0.280	28.8	94	1.98	1.00	...
	3	0.024	31.3	93	2.34	1.00	...
0809−493	1	0.336	0.0	...	0.86	1.00	...
	2	0.027	7.6	105	2.94	1.00	...
0826−373	1	0.820	0.0	...	0.65	1.00	...
	2	0.138	2.6	118	0.29	1.00	...
0842−754	1	0.056	0.0	...	0.05	1.00	...
	2	0.073	7.1	2	5.66	1.00	...
0920−397	1	1.231	0.0	...	0.88	0.63	−13
	2	0.027	7.4	−114	0.44	1.00	...
0925−203	1	0.210	0.0	...	0.38	1.00	...
	2	0.022	3.9	−18	0.38	1.00	...
1048−313	1	0.253	0.0	...	0.27	1.00	...
	2	0.064	4.2	−148	0.52	1.00	...
1057−797	1	1.282	0.0	...	0.44	1.00	...
1101−325.....	1	0.339	0.0	...	0.71	0.43	11
1105−680.....	1	0.572	0.0	...	0.49	1.00	...
	2	0.251	4.2	51	0.60	1.00	...
1237−101	1	0.586	0.0	...	0.33	1.00	...
	2	0.163	3.3	−79	0.42	1.00	...
1237−113.....	1	0.065	0.0	...	0.19	1.00	...
1251−713	1	0.412	0.0	...	0.42	1.00	...
1352−104	1	1.054	0.0	...	0.48	0.62	−62
1435−218	1	0.422	0.0	...	0.58	1.00	...
	2	0.078	21.5	−58	0.45	1.00	...
1508−055	1	0.598	0.0	...	0.41	0.66	−62
1519−273	1	1.420	0.0	...	0.55	0.46	−38
1540−828	1	0.074	0.0	...	2.49	1.00	...
	2	0.079	36.7	−96	2.46	1.00	...
	3	0.050	75.9	−97	2.67	1.00	...
1549−790	1	0.731	0.0	...	0.69	1.00	...
	2	0.379	4.0	−129	1.44	1.00	...
1604−333	1	0.198	0.0	...	0.56	0.36	−50
1610−771	1	0.488	0.0	...	2.32	1.00	...
	2	0.409	38.1	78	2.70	1.00	...
	3	0.263	75.4	84	3.08	1.00	...
1729−373	1	0.231	0.0	...	0.37	1.00	...
	2	0.194	0.8	10	0.37	1.00	...
	3	0.130	10.6	−77	0.89	1.00	...
1748−253	1	0.191	0.0	...	3.59	0.58	26
1903−802	1	0.195	0.0	...	0.32	1.00	...
	2	0.040	3.4	97	0.00	1.00	...

TABLE 3—*Continued*

Source	Component No.	S (Jy)	r (mas)	θ (deg)	a (mas)	b/a	ϕ (deg)
1908−201	1	1.305	0.0	...	0.69	0.49	−43
	2	0.130	3.4	36	0.66	1.00	...
2000−330	1	0.332	0.0	...	0.46	1.00	...
	2	0.136	2.1	−37	0.23	1.00	...
2005−489	1	0.551	0.0	...	0.66	1.00	...
	2	0.066	2.4	−134	2.24	1.00	...
2054−377	1	0.417	0.0	...	0.30	1.00	...
	2	0.017	4.3	−64	0.01	1.00	...
2059−786	1	0.178	0.0	...	0.16	1.00	...
	2	0.024	5.0	131	0.00	1.00	...
2109−811.....	1	0.335	0.0	...	0.39	1.00	...
2149−307	1	0.781	0.0	...	0.49	1.00	...
	2	0.062	8.7	−100	0.00	1.00	...
2211−388.....	1	0.172	0.0	...	0.79	1.00	...
	2	0.069	3.5	−160	0.32	1.00	...
2227−399	1	0.315	0.0	...	0.42	1.00	...
	2	0.030	3.3	−167	0.34	1.00	...
2245−328	1	0.208	0.0	...	0.24	1.00	...
2259−375	1	0.154	0.0	...	3.88	1.00	...
2300−307	1	0.080	0.0	...	0.40	1.00	...
	2	0.006	3.3	124	0.00	1.00	...

NOTE.—Table 3 is also available in machine-readable form in the electronic edition of the *Astronomical Journal*.

[a] The models fitted to the visibility data are of Gaussian form with flux density S and FWHM major axis a and minor axis b, with major axis in position angle ϕ (measured north through east). Components are separated from the (arbitrary) origin of the image by an amount r in position angle θ, which is the position angle (measured north through east) of a line joining the components with the origin.

northern hemisphere sources, Fey & Charlot (2000) found correlations between the observed radio structure and the astrometric position accuracy and stability of the observed sources. These correlations indicated that the more extended sources have larger position uncertainties and are less positionally stable than the more compact sources. On average they found that structure index 3 and 4 sources had a positional uncertainty a factor of 2 worse than structure index 1 and 2 sources.

Following the analysis of Fey & Charlot (1997, 2000), we have calculated a structure index for all 111 of our observed sources, and the results are presented in Table 5. It should be noted that the structure index calculation has been done using the source models derived from our S2 data assuming that they were observed at the same four frequency channels as those used for VLBA astrometric observations and applying the same X-band scaling factor (1.08) for consistency with previous results (Fey & Charlot 1997, 2000), even though the S2 recording system used for the observations reported here used only a single frequency channel. This assumes only that the sources are flat spectrum and have the same structure at each of the four VLBA frequency channels. We feel that this is not an unreasonable assumption for active galactic nuclei. The distribution of the structure index as a function of ICRF category is shown in Figure 3. The sources were originally defined into three categories by Ma et al. (1998) as follows: defining sources that set the direction of the ICRF axes, candidate sources that may be considered for future promotion to defining sources, and "other" sources that were determined to be unsuitable for the definition of a high-accuracy reference frame. Starting with the first extension to the ICRF (ICRF-Ext.1; Fey et al. 2004c), a fourth category of "new" sources was defined to account for source positions added since the definition of the ICRF.

TABLE 4

PHYSICAL CHARACTERISTICS OF SOURCES

Source	Optical ID[a]	Redshift	Visual Magnitude[b]
0047−579	Q	1.797	18.5
0056−572	Q	0.018	18.3
0220−349	Q	1.490	22.0
0252−549	Q	0.539	19.3
0335−364	Q	1.541	18.0
0400−319	Q	1.288	19.5
0402−362	Q	1.417	17.17
0405−385	Q	1.285	18.0
0454−810	Q	0.444	19.6
0522−611.....	...	...	...
0530−727	...	...	...
0738−674	Q	1.663	19.8
0743−673	Q	1.510	16.37
0809−493	...	...	24.0
0826−373	...	...	...
0842−754	Q	0.521	18.9
0920−397	Q	0.591	18.8
0925−203	Q	0.348	16.4
1048−313	Q	1.429	18.5
1057−797	Q	...	19.0
1101−325.....	Q	0.355	16.3
1105−680.....	Q	0.588	18.4
1237−101	Q	0.752	18.1
1237−113.....	G	0.003	8.98
1251−713	...	...	...
1352−104	Q	0.332	18.4
1435−218	Q	1.187	17.9
1508−055	...	...	...
1519−273	Q	0.071	18.5
1540−828	...	...	...
1549−790	...	...	...
1604−333	Q?	...	20.5*B*
1610−771	Q	1.710	19.0
1729−373	...	...	...
1748−253	...	...	...
1903−802	Q	0.500	19.0
1908−201	Q		
2000−330	Q	3.773	19.0
2005−489	Q	0.071	15.3
2054−377	Q	1.071	17.5
2059−786	Q	...	21.0
2109−811.....	G	...	20.0
2149−307	Q	2.345	18.4
2211−388.....	G	...	22.0
2227−399	Q	0.323	18.5
2245−328	Q	2.268	18.6
2259−375	...	...	...
2300−307	Q	...	16.0

[a] (Q) QSO; (G) galaxy.

[b] The letters after the magnitudes indicate the bandpass to which the magnitude applies. For example, *U, B, V, R,* and *I* are for the standard Johnson and/or Cousins magnitudes. If no letter is given, the filters are not currently specified in NED. These magnitudes should be regarded as indicative only.

As can be seen in Figure 3, only 38 sources (approximately 35% of the sources in our sample) have a structure index of either 1 or 2, an indication of compact or very compact structures. The remaining 72 sources (one of the 69 sources reported in Paper I was not an ICRF source and is not included in the analysis here) with a structure index of either 3 or 4 have more extended emission structures. As such structures are more likely to affect the observed VLBI bandwidth synthesis delays, Fey & Charlot (1997) recommended that such sources, especially those

TABLE 5

SOURCE STRUCTURE INDEX

Source	τ_{mean} (ps)	τ_{rms} (ps)	τ_{max} (ps)	τ_{median} (ps)	Structure Index	Epoch[a]
0008−264	2.6	3.4	15.5	2.1	1	B
0047−579	31.9	40.7	188.8	26.2	3	D
0056−572	209.9	354.2	4290.8	100.3	4	E
0118−272	135.8	181.6	1619.8	101.0	4	B
0130−171	8.2	10.6	52.2	6.7	2	A
0131−522	6.3	8.5	49.2	4.8	2	B
0135−247	33.9	90.3	1940.0	13.9	3	B
0147−076	28.7	38.4	235.7	22.0	3	B
0150−334	100.9	175.4	2665.4	58.6	4	B
0202−765	23.2	32.0	145.9	16.5	3	B
0208−512	6.7	9.3	42.6	4.2	2	A
0220−349	16.1	23.2	139.1	10.4	3	D
0230−790	102.3	261.9	3279.9	39.7	4	B
0252−549	127.8	239.5	2656.2	67.4	4	E
0252−712	913.6	1280.4	6458.7	654.6	4	A
0308−611	2.0	2.6	12.6	1.6	1	B
0332−403	2.5	3.2	16.3	2.1	1	A
0332−403	4.4	6.5	58.6	2.9	1	B
0335−364	46.8	106.6	2165.4	19.6	3	D
0338−214	25.3	74.3	1659.2	10.1	3	B
0400−319	6.6	8.5	52.0	5.3	2	D
0402−362	5.6	7.8	41.8	3.9	2	D
0405−385	80.5	169.6	3278.1	37.5	4	D
0451−282	88.5	138.5	735.7	44.5	4	B
0454−463	1.7	2.2	7.9	1.3	1	A
0454−810	6.4	8.0	31.1	5.4	2	C
0506−612	12.8	18.5	58.2	7.2	2	A
0511−220	11.7	22.4	278.4	7.6	2	B
0521−365	33.0	48.4	219.4	20.0	3	A
0522−611	6.8	8.8	36.0	5.4	2	A
0522−611	14.3	18.6	76.9	11.2	3	C
0528−250	12.9	17.6	82.8	9.3	2	B
0530−727	71.9	183.4	2880.5	29.1	3	E
0537−286	5.0	7.5	40.6	3.1	2	B
0614−349	53.2	139.7	3417.4	27.0	3	B
0637−337	15.4	24.2	87.8	8.3	2	A
0637−752	80.6	149.1	2081.9	44.4	4	A
0727−365	202.3	334.4	2488.3	111.5	4	B
0736−332	84.2	170.1	3262.2	44.2	4	B
0738−674	17.6	24.6	127.5	12.1	3	A
0738−674	13.3	18.1	123.8	10.1	3	C
0743−673	55.6	73.7	360.2	41.8	4	D
0809−493	80.1	189.8	2375.4	28.0	3	D
0823−223	3.6	5.0	30.5	2.6	1	B
0823−500	438.5	595.7	3910.8	311.5	4	A
0826−373	76.0	156.7	2728.7	39.2	4	E
0834−201	6.6	13.0	317.1	4.5	2	B
0842−754	150.5	203.7	3662.0	114.0	4	E
0920−397	31.3	51.9	545.5	18.5	3	D
0925−203	12.9	18.7	83.7	8.2	2	B
0925−203	56.4	105.5	1043.3	26.3	3	D
1004−500	13.0	19.0	79.8	8.3	2	A
1020−103	39.6	52.1	341.6	30.8	4	B
1032−199	53.2	127.3	1894.4	27.8	3	B
1039−474	194.1	369.1	4070.1	103.2	4	A
1048−313	70.2	103.9	696.1	44.8	4	E
1057−797	14.9	21.9	129.4	9.7	2	A
1057−797	32.7	44.5	335.3	26.8	3	C
1101−325	20.2	31.8	166.5	9.9	2	D
1105−680	165.2	279.5	2020.0	87.5	4	D
1143−245	67.8	130.2	1619.6	35.8	4	B
1221−829	40.5	173.8	1624.3	6.8	2	A
1226−028	10.0	12.8	78.6	8.2	2	B
1237−101	103.6	226.5	1979.4	43.2	4	E

TABLE 5—*Continued*

Source	τ_{mean} (ps)	τ_{rms} (ps)	τ_{max} (ps)	τ_{median} (ps)	Structure Index	Epoch[a]
1237−113	62.0	230.4	4919.0	25.9	3	E
1251−713	11.4	16.2	191.0	8.1	2	D
1255−316	24.1	77.8	1982.0	9.5	2	B
1320−446	120.1	259.0	2277.6	43.3	4	A
1349−439	5.7	8.0	31.1	3.8	2	A
1352−104	3.7	4.9	18.5	3.0	2	D
1424−418	3.3	4.2	19.0	2.8	1	A
1435−218	98.2	204.4	4208.6	54.3	4	E
1508−055	7.7	10.0	39.1	6.1	2	D
1514−241	138.0	208.5	1824.6	93.1	4	A
1519−273	0.1	0.2	0.4	0.1	1	A
1519−273	1.1	1.4	5.9	0.9	1	B
1519−273	2.9	4.0	27.9	2.1	1	D
1540−828	1385.5	1667.0	5000.4	1313.0	4	E
1549−790	181.2	314.0	2105.2	82.5	4	D
1604−333	15.4	36.4	625.5	8.1	2	D
1610−771	778.5	1152.3	6086.6	502.9	4	E
1622−297	56.3	100.9	719.9	26.6	3	A
1622−297	71.9	180.2	2862.1	23.1	3	B
1647−296	5.7	7.7	48.2	4.3	2	B
1657−261	3.0	4.0	26.4	2.3	1	B
1718−649	271.6	425.2	2697.2	161.1	4	A
1729−373	200.8	340.3	2669.9	129.5	4	E
1733−565	13.6	17.5	84.3	11.1	3	B
1748−253	35.9	51.4	1814.8	26.5	3	D
1758−651	2.9	3.7	17.5	2.3	1	B
1814−637	333.3	741.2	5858.2	168.2	4	A
1817−254	23.4	31.1	147.0	17.2	3	B
1903−802	102.7	165.3	2227.3	63.9	4	E
1908−201	16.9	23.6	79.8	11.4	3	A
1908−201	19.4	27.5	113.7	12.8	3	B
1908−201	29.8	60.1	1652.6	16.6	3	D
1920−211	9.8	13.3	58.4	7.0	2	A
1934−638	936.3	1290.8	5584.4	697.1	4	A
1934−638	631.5	1007.2	5583.2	397.9	4	B
1954−388	1.7	2.2	9.3	1.4	1	A
2000−330	62.0	117.3	1898.3	36.9	4	D
2005−489	96.7	221.3	2351.3	33.8	4	D
2037−253	54.4	160.5	1733.7	14.6	3	B
2052−474	14.7	19.2	87.4	11.5	3	A
2054−377	21.6	41.7	1047.7	11.1	3	E
2059−786	47.6	63.9	244.4	34.5	4	C
2101−490	16.8	25.0	375.1	11.5	3	B
2109−811	34.3	87.3	1220.1	19.9	3	C
2115−305	39.6	53.4	315.9	29.8	3	B
2149−307	76.5	132.6	2171.1	48.2	4	D
2152−699	131.3	263.4	2425.8	59.0	4	B
2155−304	6.1	7.9	34.2	4.9	2	A
2211−388	117.7	221.8	2876.5	59.2	4	E
2227−399	53.6	95.5	1089.0	26.3	3	E
2229−172	28.2	44.7	288.6	16.1	3	B
2245−328	10.1	13.1	67.4	8.1	2	D
2259−375	215.6	381.3	4860.1	86.6	4	E
2300−307	55.6	129.4	2308.6	26.1	3	D
2300−683	4.8	6.5	32.8	3.7	2	B
2312−319	17.7	24.9	98.1	11.6	3	B
2331−240	37.2	62.0	389.1	17.7	3	B
2353−686	11.4	15.6	177.0	8.8	2	B

NOTE.—Table 5 is also available in machine-readable form in the electronic edition of the *Astronomical Journal*.

[a] The labels A, B, C, D, and E refer to epochs 2002 July 16, 2002 November 14, 2003 June 20, 2003 November 23, and 2004 April 18, respectively.

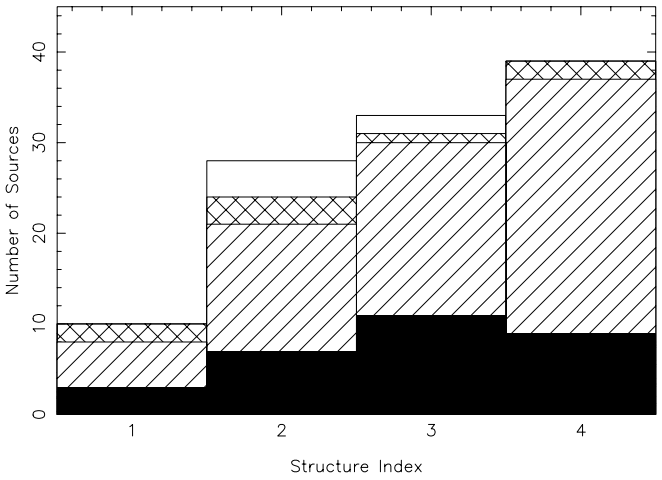

FIG. 3.—Distribution of the structure index at the X band for 110 southern hemisphere ICRF sources (one of the 69 sources reported in Paper I was not an ICRF source and is not included in the analysis here). The individual structure indices are available from Table 5. In the case of multiple-epoch observations, the structure indices from the most recent epoch were used. The filled portion of the histogram represents ICRF defining sources, the hatched portion represents candidate sources, the cross-hatched portion represents "other" sources (deemed unsuitable for defining the ICRF), and the open portion represents new sources in ICRF Extension 1.

with a structure index of 4 (approximately 35% of the sources in our sample), should be avoided in astrometric and geodetic VLBI experiments requiring the highest accuracy.

At 8.4 GHz, Fey & Charlot (2000) found that approximately 60% of their sample had a structure index of either 1 or 2, while the remaining 40% had a structure index of either 3 or 4. Our results for southern hemisphere sources show a larger fraction of structure index 3 and 4 sources than those of Fey & Charlot (2000), whose sample consisted of mostly northern hemisphere sources. This could possibly be attributed to selection effects, limitations in the images (mostly due to limited [*u, v*]-coverage), or the smaller size of our southern hemisphere sample. A more detailed analysis comparing northern and southern sources will be undertaken when we have completed observations of all the southern hemisphere ICRF sources.

5. SUMMARY

Milliarcsecond images of 48 southern hemisphere ICRF sources are presented. Of the 48 sources presented in this paper, just under one-third show a single compact component. In general, these should be well suited for reference frame use. The remainder show extended structure in the form of multiple compact components but have most of their flux in a central component. Usually, these sources are less well suited for high-accuracy reference frame use. This is quantified by our structure index calculation, which shows that about two-thirds of our sources are of relatively poor astrometric quality. Taking into account the structure for sources with structure index 3 and 4 in astrometric measurements should improve the astrometric quality of these sources. This should be done in future definitions of the ICRF.

The imaging results presented here and in Paper I represent the most extensive milliarcsecond VLBI survey of southern hemisphere ICRF sources to date and as such provide a valuable tool for the investigation of a wide range of physical phenomena associated with these objects. Observations of additional southern hemisphere ICRF sources will be reported as they are reduced and analyzed. We expect to be able to observe all sources at least twice and perhaps three times over the life of this project. This should allow us to produce time-dependent source models and evaluate the intrinsic structure and variability of the observed sources.

The hard work of the support and observing staff at all participating stations, as well as at the ATNF correlator, is gratefully acknowledged. This research has made use of the United States Naval Observatory Radio Reference Frame Image Database. This research has made use of the NASA/IPAC Extragalactic Database, which is operated by the Jet Propulsion Laboratory, California Institute of Technology, under contract with the National Aeronautics and Space Administration.

REFERENCES

Bridle, A. H., & Greisen, E. W. 1994, AIPS Memo 87, The NRAO AIPS Project: A Summary (Socorro: NRAO), ftp://ftp.aoc.nrao.edu/pub/software/aips/TEXT/PUBL/AIPSMEMO87.PS
Cannon, W. H., et al. 1997, Vistas Astron., 41, 297
Charlot, P. 1990, AJ, 99, 1309
Fey, A. L., & Charlot, P. 1997, ApJS, 111, 95
———. 2000, ApJS, 128, 17
Fey, A. L., Ojha, R., Reynolds, J. E., Ellingsen, S. P., McCulloch, P. M., Jauncey, D. L., & Johnston, K. J. 2004a, AJ, 128, 2593
Fey, A. L., et al. 2004b, AJ, 127, 1791
———. 2004c, AJ, 127, 3587
Greisen, E. W. 1988, AIPS Memo 61, The Astronomical Image Processing System (Socorro: NRAO), ftp://ftp.aoc.nrao.edu/pub/software/aips/TEXT/PUBL/AIPSMEMO61.PS
Johnston, K. J., Russell, J., de Vegt, C., Hughes, J., Jauncey, D. L., White, G., & Nicolson, G. 1988, in IAU Symp. 129, The Impact of VLBI on Astrophysics and Geophysics, ed. M. J. Reid & J. M. Moran (Dordrecht: Kluwer), 317
Johnston, K. J., et al. 1995, AJ, 110, 880
Kovalevsky, J., et al. 1997, A&A, 323, 620
Ma, C., Shaffer, D. B., de Vegt, C., Johnston, K. J., & Russell, J. L. 1990, AJ, 99, 1284
Ma, C., et al. 1998, AJ, 116, 516
Ojha, R., Fey, A. L., Johnston, K. J., Jauncey, D. L., Tzioumis, A. K., & Reynolds, J. E. 2004a, AJ, 127, 1977
Ojha, R., et al. 2004b, AJ, 127, 3609 (Paper I)
Pearson, T. J., & Readhead, A. C. S. 1984, ARA&A, 22, 97
———. 1988, ApJ, 328, 114
Perryman, M. A. C., et al. 1997, A&A, 323, L49
Preston, R. A., et al. 1989, AJ, 98, 1
Reynolds, J. E., Jauncey, D. L., Russell, J. L., King, E. A., McCulloch, P. M., Fey, A. L., & Johnston, K. J. 1994, AJ, 108, 725
Russell, J. L., et al. 1994, AJ, 107, 379
Shen, Z.-Q., et al. 1997, AJ, 114, 1999
———. 1998, AJ, 115, 1357
Shepherd, M. C. 1997 in ASP Conf. Ser. 125, Astronomical Data Analysis Software and Systems VI, ed. G. Hunt & H. E. Payne (San Francisco: ASP), 77
Taylor, G. B., Vermeulen, R. C., Readhead, A. C. S., Pearson, T. J., Henstock, D. R., & Wilkinson, P. N. 1996, ApJS, 107, 37
Wilson, W. E., Roberts, P. P., & Davis, E. R. 1995, in Proc. 4th APT Workshop, Sydney, ed. E. A. King (Sydney: ATNF), 16